ACS OMEGA

Open Access



http://pubs.acs.org/journal/acsodf

Article

# One-Pot Synthesis of Tannic Acid-Au Nanoparticles for the Colorimetric Determination of Hydrogen Peroxide and Glucose

Chun-Hsiang Peng,[⊥] Tsung-Yuan Wang,[⊥] Chen-Yu Chueh, Tsunghsueh Wu, Jyh-Pin Chou, Mei-Yao Wu, and Yang-Wei Lin*

Cite This: *ACS Omega* 2024, 9, 38217−38226

Read Online

ACCESS | Metrics & More | Article Recommendations | Supporting Information

**ABSTRACT:** This study introduces a novel one-pot method employing tannic acid (TA) to synthesize stable gold nanoparticles (TA-AuNPs), which are characterized using transmission electron microscopy, X-ray powder diffraction, and Fourier transform infrared spectroscopy. We apply these TA-AuNPs in a newly developed colorimetric assay for hydrogen peroxide ($H_2O_2$) detection that utilizes the oxidation of iodide ($I^-$) on TA-AuNPs, leading to a detectable yellow color change in the solution. The reaction kinetics are captured by the rate equation $R = 0.217[KI]^{0.61}[H_2O_2]^{0.69}$. The possible sensing mechanism was proposed through density functional theory calculations. At the optimum conditions, the proposed TA-AuNPs/$I^-$ system demonstrated a linear relationship between $H_2O_2$ concentration and absorbance intensity ($\lambda$ = 350 nm) and achieved a limit of detection (LOD) of 7.33 $\mu$M. Furthermore, we expand the utility of this approach to glucose detection by integrating glucose oxidase into the system, resulting in a LOD of 10.0 $\mu$M. Application of this method to actual urine samples yielded spiked recovery rates ranging from 96.6−102.0% and relative standard deviations between 3.00−8.34%, underscoring its efficacy and potential for real-world bioanalytical challenges.

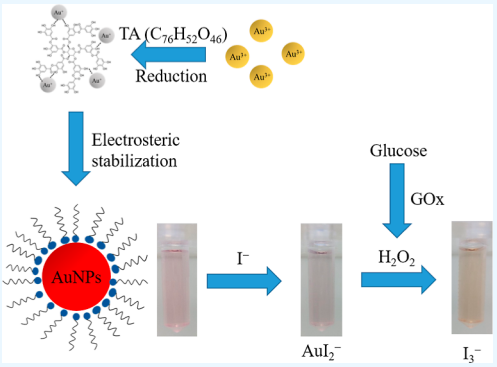


## 1. INTRODUCTION

Hydrogen peroxide ($H_2O_2$) detection is essential due to its everyday use as a disinfectant in the food industry, where its residual presence can pose health risks.[1−3] Existing $H_2O_2$ detection methods include electroanalytical techniques, liquid chromatography, and fluorescence spectroscopy, which, while selective and sensitive, suffer from high operational costs, complexity, and the need for expensive equipment.[4−8] These drawbacks limit their applicability in practical scenarios. In contrast, colorimetric assays are more user-friendly, providing easy-to-interpret visual results without sophisticated instrumentation, making them better suited for real-world applications.[9−11] Furthermore, glucose monitoring is critical in diabetes management, affecting millions of people globally. Traditional glucose monitoring methods, mainly blood tests, are invasive and inconvenient for frequent tracking. The need for accurate, noninvasive, and user-friendly glucose detection methods is thus pressing.[12−17]

Gold nanoparticles (AuNPs) are renowned for their distinctive features, including minimal size, extensive surface area, and localized surface plasmon resonance (SPR), which underscore their exceptional sensing capabilities, especially in colorimetric assays.[18−20] Traditional synthesis methods, such as sodium citrate reduction, depend on particle aggregation for detection yet are prone to inaccuracies due to electrolyte-induced aggregation. To address these limitations, researchers have explored Au nanozymes, developing a colorimetric sensor for $H_2O_2$ and glucose that employs AuNPs synthesized through a $MoO_3$-nanosheet-assisted photochemical method, eliminating the need for surface modification.[21] This sensor employs $MoO_3$ residues and Mo(VI) ions as peroxidase mimics, facilitating iodine production from iodate in the presence of $H_2O_2$ or glucose oxidase (GOx), causing a noticeable color change. It exhibits linear responses for $H_2O_2$ (40−380 $\mu$M, $R^2$ = 0.99) and glucose (100−1000 $\mu$M, $R^2$ = 0.98) with low detection limits (0.55 $\mu$M for $H_2O_2$ and 0.45 $\mu$M for glucose) and has shown promising results in glucose analysis in water chestnuts with recoveries of 100−108%. Another study reports the creation of positively charged AuNPs [(+)AuNPs] for $H_2O_2$ detection, synthesized via an electrochemically active biofilm.[22] These (+)AuNPs, characterized by their significant intrinsic peroxidase-like activity, offer a simple, rapid, and sensitive method for $H_2O_2$ detection within a linear range of $1.0 \times 10^{-3}$ to $2.5 \times 10^{-3}$ M. While novel, the synthesis of these AuNPs relies on specific chemical

Received: June 22, 2024
Revised: July 31, 2024
Accepted: August 14, 2024
Published: August 23, 2024

additives, which may limit their broader application. Recently, Li's group innovated a AuNP-based colorimetric microneedle (MN) patch featuring minimally invasive sampling and real-time interstitial fluid (ISF) glucose analysis capabilities.[23] This patch can rapidly absorb substantial amounts of skin ISF, extracting up to 60.2 mg within 10 min in vitro. Structured in two layers, the tip layer contains AuNPs with GOx-like activity that initiates glucose oxidation from the ISF, producing $H_2O_2$. Concurrently, the backing layer, containing encapsulated horseradish peroxidase, facilitates the oxidation of 3,3′,5,5′-tetramethylbenzidine (TMB) by $H_2O_2$, resulting in oxTMB and a detectable color change. The glucose levels in the ISF are visually interpretable and can be quantitatively analyzed by using ImageJ software. In vivo tests demonstrated that the colorimetric MN patch effectively distinguishes between normal and hyperglycemic blood sugar levels. However, the complexity of the patch's production limits its widespread application. In addition, Wang's group developed a series of hierarchically organized AuNPs (Au HOPs-X) that exhibit enhanced peroxidase-like catalytic activity.[24] This was achieved through the in situ reduction of Au-thiolate complexes within the initial Au HOPs, significantly enhancing their enzymatic functionality. The increased catalytic activity is attributed to two primary factors: converting Au-thiolate complexes on the particle surface into active AuNPs, leading to a rise in active $Au^0$ content, and an expansion in the specific surface area of the Au HOPs-X. Among them, Au HOPs-10 stood out for its superior catalytic performance and was subsequently paired with GOx to establish a glucose concentration standard curve. The observable color transitions in the solutions were documented by using smartphone photography, facilitating the rapid determination of glucose levels by correlating solution saturation with glucose concentration. However, the synthesis process of Au HOPs-X was time-consuming.

This study uses tannic acid (TA) as a reducing and stabilizing agent in a one-pot synthesis method to create TA-synthesized AuNPs (TA-AuNPs). This innovative approach eliminates the need for purification, streamlining the production process. Our novel sensor based on TA-AuNPs revolutionizes colorimetric assays by enhancing the detection precision without relying on particle aggregation. The sensor detects $H_2O_2$ through a redox reaction with iodide ($I^-$) adsorbed on TA-AuNPs, causing a color change from pink to yellow and altering the visible light absorption spectrum. Expanding the utility of the sensor, we apply it to noninvasive glucose monitoring by leveraging $H_2O_2$ production from GOx in glucose solutions. This innovative approach offers a straightforward, cost-effective, and noninvasive method for sensitive and selective detection of $H_2O_2$ and glucose. It holds significant promise for advancing environmental monitoring, food safety, and diabetic care, establishing a new standard in bioanalytical methodologies.

## 2. MATERIALS AND METHODS

**2.1. Chemicals.** The experimental reagents used in this study included sodium tetrachloroaurate(III) dihydrate ($NaAuCl_4{\cdot}2H_2O$), TA, KI, $H_2O_2$, D-(+)-glucose, GOx, sucrose, beta-D-(−)-fructose, D-(+)-mannose, xylitol, sodium citrate tribasic dihydrate, ascorbic acid (AA), uric acid (UA), NaCl, KCl, $MgCl_2$, $CaCl_2$, bovine serum albumin (BSA), glutathione (GSH), and glycine (GLY). All chemicals were obtained from Sigma-Aldrich (St. Louis, MO, USA) and were of analytical grade or the highest available purity. Milli-Q deionized water was used exclusively for all of the experimental procedures.

**2.2. Characterization.** The characterization of the synthesized TA-AuNPs was conducted by using comprehensive analytical methods. The optical properties were assessed by UV−visible (UV−vis) spectroscopy using an Evolution 200 UV−vis spectrophotometer (ThermoFisher Scientific, NY, USA). The crystalline structure was determined via X-ray diffraction (XRD) on a LabX XRD-6000 diffractometer (Shimadzu Corporation, Kyoto, Japan). Organic functional groups on the TA-AuNPs were identified through Fourier transform infrared spectroscopy with an Agilent Cary 600 series instrument (Agilent Technologies, California, USA). Morphology and microstructure examinations were performed using transmission electron microscopy (TEM) on a JEOL-1200EX II (JEOL Ltd., Tokyo, Japan). A dynamic light scattering (DLS) spectrophotometer (SZ-100, Horiba, Kyoto, Japan) was used to measure the hydrodynamic diameter and zeta potential of the prepared TA-AuNPs under different conditions. The surface composition was confirmed by X-ray photoelectron spectroscopy (XPS) using a VG ESCA210 (VG Scientific, West Sussex, UK).

**2.3. One-Pot Synthesis of TA-AuNPs.** This study synthesized a series of TA-AuNP solutions under varying conditions for comparative analysis. Five 50 mL sample bottles were prepared, each containing 50 mL of $NaAuCl_4$ (130 $\mu$M). The solutions were brought to a boil, after which 2 mL of TA solution, at different concentrations (0.6, 1.2, 6.0, 30.0, and 60.0 mM), was added to each bottle. The mixtures were maintained at a boil for two more minutes to ensure a thorough reaction. Upon cooling to room temperature, the resultant TA-AuNP solutions, differing in TA concentrations, were methodically analyzed using UV−vis spectroscopy to assess their optical properties and nanoparticle formation. For clarity, TA-AuNPs synthesized with TA concentrations of 0.6, 1.2, 6.0, 30.0, and 60.0 mM are designated as TA-AuNPs-1, TA-AuNPs-2, TA-AuNPs-3, TA-AuNPs-4, and TA-AuNPs-5, respectively. We replaced TA with sodium citrate (2 mL, 6.0 mM) to prepare sodium citrate-stabilized AuNPs (SC-AuNPs). The mixtures were maintained at a boiling temperature for 7 min to ensure a thorough reaction, resulting in the characteristic red color of the SC-AuNP solution.

**2.4. Steady-State Kinetic Study.** In this study, TA-AuNPs-3 (the concentration of the freshly prepared TA-AuNPs-3 was estimated to be $2.2 \times 10^{-6}$ M) were prepared at a concentration of $1.1 \times 10^{-7}$ M. For each assay, 0.9 mL of deionized water, 0.5 mL of KI at varying concentrations (0.75, 1.5, 3.0, 4.0, and 6.0 M), and 0.5 mL of $H_2O_2$ (25 mM) were mixed in 2.0 mL microcentrifuge tubes. The mixtures were then subjected to different reaction times and analyzed by using UV−vis spectroscopy. The initial rate of $I_3^-$ formation was determined based on the absorbance peak at 350 nm. A log−log plot of the rate versus the KI concentration was constructed. A linear fitting was performed to determine the reaction order for KI.[25,26] Similarly, TA-AuNPs-3 were prepared at the same concentration, mixed with 0.9 mL of deionized water, 0.5 mL of 0.75 M KI, and 0.5 mL of $H_2O_2$ at various concentrations (0.8, 1.13, 1.31, 1.50, and 1.88 mM). The solutions were analyzed after different reaction times using UV−vis spectroscopy. The initial rate of $I_3^-$ formation was calculated from the absorbance at 350 nm. A log−log plot of the rate against the $H_2O_2$ concentration was then constructed, and linear fitting was used to establish the reaction order


https://doi.org/10.1021/acsomega.4c05826
ACS Omega 2024, 9, 38217−38226

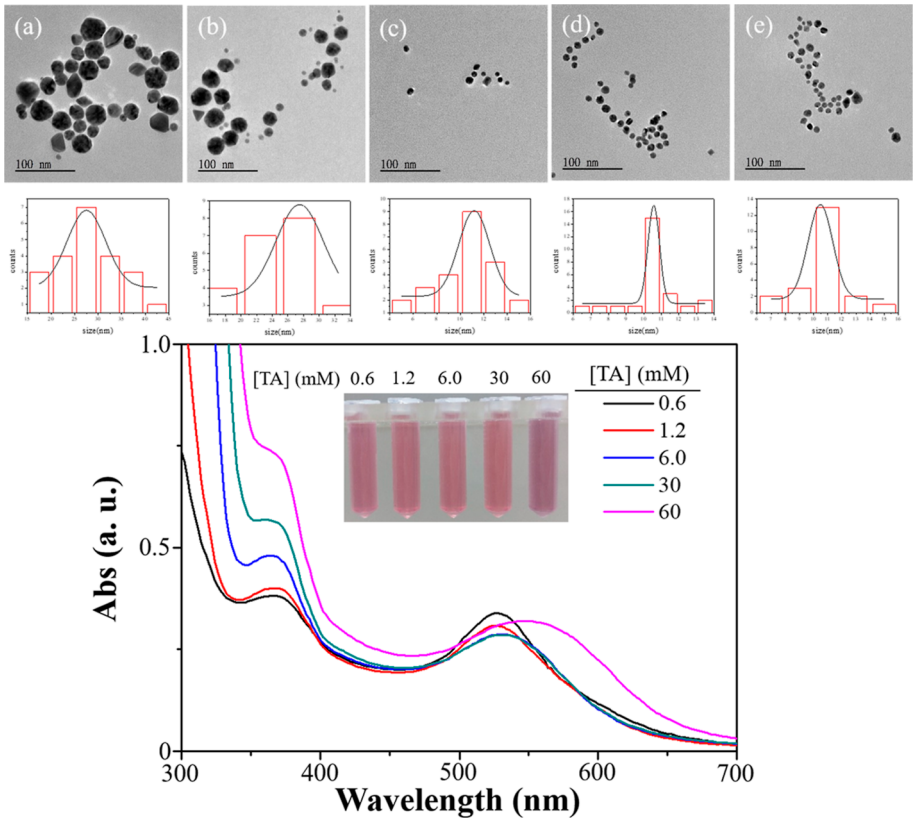


**Figure 1.** TEM images, size distribution histograms, and UV−vis spectra showcasing TA-AuNPs synthesized at varying TA concentrations: (a) 0.6, (b) 1.2, (c) 6.0, (d) 30, and (e) 60 mM. Inset: photographic representations of the respective AuNP solutions. Photograph courtesy of Chun-Hsiang Peng. Copyright 2024.

concerning $H_2O_2$. Upon determination of the reaction orders for KI and $H_2O_2$, the rate constants for various conditions were calculated by inserting the concentrations of KI and $H_2O_2$ into the rate equation. The average of these rate constants was taken as the overall rate constant '*k*' for the reaction, thus deriving the rate equation for the $H_2O_2$ detection system.[25,26]

**2.5. Simulated Adsorption Energy for TA-AuNPs/KI and TA-AuNPs/$H_2O_2$.** All spin-polarized periodic density functional theory (DFT) calculations were performed using the Vienna ab initio simulation package (VASP).[27,28] The generalized gradient approximation with the functional proposed by Perdew, Burke, and Enzerhof exchange−correlation functional was used together with a plane-wave basis set with a kinetic cutoff energy of 400 eV.[29] The electron ion−core interactions were described by the projector augmented wave method.[30,31] The dispersion energy correction was considered using the DFT-D3 method by Grimme.[32] In the present work, the convergence threshold was set to $10^{-4}$ eV for electronic optimization, and the force convergence was set to 0.01 eV/Å for structural optimization. Bulk Au adopted the face-centered cubic (fcc) structure. In the bulk Au calculation, the Brillion zone was sampled using (8 × 8 × 8) Monkhorst−Pack *k*-point mesh.[33] The optimum unit cell of the Au crystal, as determined by XRD findings, is shown in Figures S1A, and Figure S4 depicts the reconstruction of the (111) surface within the Au solid structure. The structure of the (111)-Au surface was constructed with three molecular layer models, where the bottom three layers are fully fixed. The Brillouin zone integrations for the (111)-Au surface were performed using the (3 × 3 × 1) Monkhorst−Pack *k*-points for all structural relaxations. The following equation can summarize the calculation of the adsorption energy

$$E_{\text{Adsorption}} = E_{\text{total}} - (E_{\text{Surface}} + E_{\text{adsorbate}}) \quad (1)$$

Here, $E_{\text{Adsorption}}$ represents the energy of adsorption, indicating the energy change during the adsorption process. $E_{\text{total}}$ is the total energy of the entire system encompassing both the metal surface and the adsorbate. $E_{\text{Surface}}$ denotes the total energy of the metal surface alone, while $E_{\text{adsorbate}}$ is the total energy of the adsorbate in its isolated state. By calculating the values of $E_{\text{total}}$, $E_{\text{Surface}}$, and $E_{\text{adsorbate}}$ and substituting them into the equation, we can determine the adsorption energy, providing insights into the energetic aspects of the adsorption process.

**2.6. Determination of $H_2O_2$ and Glucose.** At room temperature, TA-AuNPs-3 were prepared at a concentration of $1.1 \times 10^{-7}$ M. Each reaction mixture contained 0.9 mL of deionized water, 0.5 mL of KI (0.75 M), and 0.5 mL of $H_2O_2$ at varying concentrations, all combined in 2 mL microcentrifuge tubes. The mixtures were left to react for 30 min, after which the resulting mixed solutions were analyzed using a UV−vis spectrophotometer to determine the changes in the absorbance peak at 350 nm, indicative of the formation of $I_3^-$. This procedure enables the evaluation of the system's response to different concentrations of $H_2O_2$, contributing to the development of a sensitive colorimetric assay for $H_2O_2$ detection.

For glucose detection, the reaction was initiated by combining 1.6 mL of glucose at varied concentrations with 0.4 mL of GOx (0.1 mg/mL) in a 2 mL microcentrifuge tube and incubating at room temperature for 60 min. In a separate 2


https://doi.org/10.1021/acsomega.4c05826
ACS Omega 2024, 9, 38217−38226

**Scheme 1. Proposed Synthesis Mechanism of AuNPs, with TA Acting as Both the Reducing Agent and Stabilizer[a]**

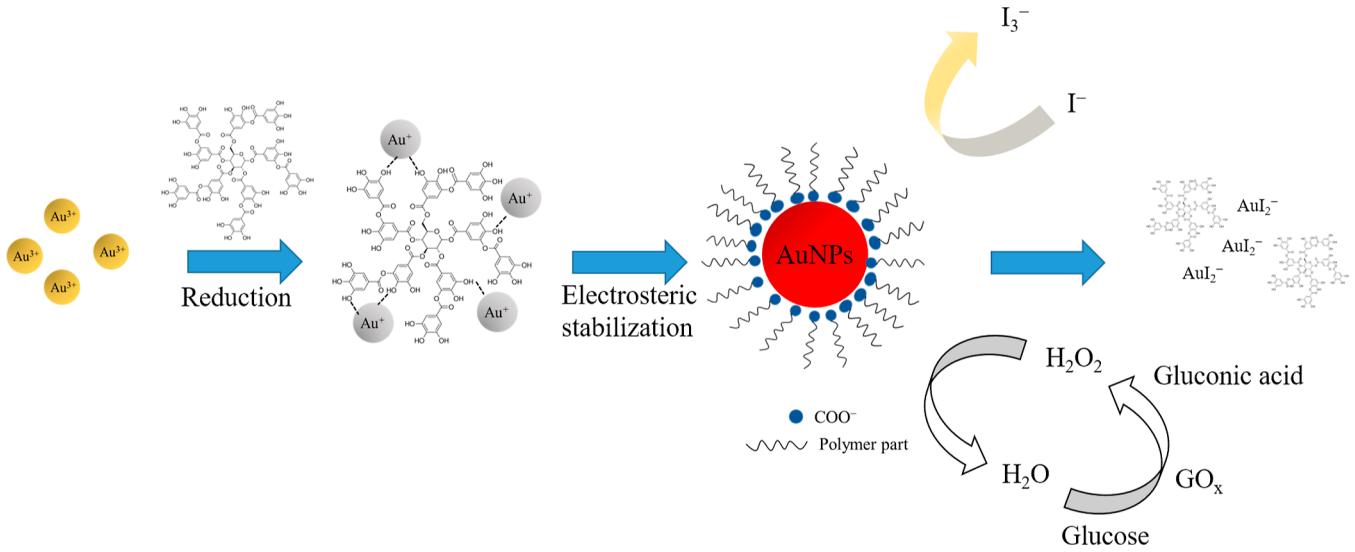


[a]The sensing mechanism for $H_2O_2$ and glucose detection is employed by the TA-AuNPs-3/KI system.

mL microcentrifuge tube, a solution of TA-AuNPs-3 was prepared at a concentration of $1.1 \times 10^{-7}$ M. 0.9 mL of deionized water and 0.5 mL of KI (0.75 M) were to this solution. 0.5 mL of the prereacted glucose-oxidase mixture was integrated into this tube. The reaction was allowed to proceed for 30 min before analyzing the solution using a UV−vis spectrophotometer.

**2.7. Pretreatment of Actual Samples.** At room temperature, human urine was diluted 10-fold and used as a solvent to prepare glucose solutions of various concentrations. At room temperature, 1.6 mL of glucose at different concentrations and 0.4 mL of GOx (0.1 mg/mL) were added to a 2 mL microcentrifuge tube and reacted for 60 min in advance. Subsequently, in another 2 mL microcentrifuge tube, TA-AuNPs-3 were prepared to a concentration of $1.1 \times 10^{-7}$ M, followed by adding 0.9 mL deionized water and 0.5 mL KI (0.75 M). Then, 0.5 mL from the above mixture was transferred into the 2 mL microcentrifuge tube. After reacting for 30 min, the mixture was analyzed using a UV−vis spectrophotometer.

## 3. RESULTS AND DISCUSSION

**3.1. Characterization of TA-AuNPs.** The UV−vis spectra of TA-AuNPs show a red shift in the SPR peak at 530 nm with increasing TA concentration, which results in an expansion of the spectral bandwidth, as depicted in Figure 1. The alternation in the SPR peak is primarily dictated by molecules adsorbing to the surface of AuNPs rather than exclusively by alterations in particle size. Figure 1 shows that the TEM analysis confirms the reduction in TA-AuNP particle size as the TA concentration escalates. The fundamental cause of this observed behavior is that at high concentrations, TA primarily serves as a reducing agent, where the rate of nucleation exceeds that of growth, culminating in smaller TA-AuNPs.[34,35] Moreover, due to the dual roles of TA as both a reducing agent and a stabilizer, increased TA concentrations lead to the encapsulation of TA-AuNPs, effectively increasing the stability of particles, as presented in Scheme 1.

Above the 6.0 mM concentration, TA extensively coats the AuNPs, rendering the particle size independent of further increases in the TA concentration, as evidenced by Figure 1 and Table 1. Table 1 also details the changes in the hydrodynamic diameter; as the concentration of TA ranges from 0.6 to 6.0 mM, the reduction in the TA-AuNP size consequently leads to a smaller hydrodynamic diameter. Nevertheless, at concentrations exceeding 6.0 mM, an excess of TA on the surface of the TA-AuNPs forms hydrogen bonds with free TA molecules in the solution, causing an increase in the hydrodynamic diameter within the concentration range of 30−60 mM, as detailed in Table 1. The zeta potential of TA-AuNPs-3 was measured across different pH values by manual titration using HCl and NaOH, as shown in Figure S1. The TA-AuNPs exhibit a very low isoelectric point (IEP), indicating that they remain negatively charged across almost the entire pH range except in highly acidic conditions (pH < 2.0). As the pH becomes more alkaline, the magnitude of the negative charge steadily decreases.

**Table 1. Variation in Particle Size and Hydrodynamic Diameter of TA-AuNPs Synthesized at Different Concentrations of TA**

| [TA] (mM) | particle size (nm)[a] | hydrodynamic diameter (nm)[b] |
|---|---|---|
| **0.6** | 27.6 ± 7.9 | 34.5 ± 1.8 |
| **1.2** | 24.5 ± 4.7 | 32.1 ± 1.8 |
| **6.0** | 10.3 ± 3.1 | 19.8 ± 1.4 |
| **30** | 10.5 ± 1.6 | 30.4 ± 5.8 |
| **60** | 10.2 ± 1.7 | 46.0 ± 2.2 |

[a]Particle size of TA-AuNPs was calculated from TEM images. [b]Hydrodynamic diameter of TA-AuNPs was measured by DLS.

Figure S2A displays the XRD results, identifying four distinct peaks at 37.80, 44.02, 64.52, and 77.60°, corresponding to the (111), (200), (220), and (311) crystal planes, respectively. This pattern confirms that the TA-AuNPs-3 have a fcc lattice structure (JCPDS: 04−0784).[35] Additionally, Figure S2B reveals identical characteristic peaks between TA-AuNPs-3 and TA, indicating the adsorption of TA onto the surface of the AuNPs. The observed peaks at 3300, 1700, 1600, 1440,


https://doi.org/10.1021/acsomega.4c05826
ACS Omega 2024, 9, 38217−38226

1200, and 760 $cm^{-1}$ correspond to O−H, C═O, aromatic rings, C−C, C−O, and C═C bonds, respectively.[36]

Based on the analysis of the AuNP synthesis using TA and sodium citrate, a distinct advantage in nanoparticle stability under varying salinity levels was identified. The TA-AuNPs-3 exhibited remarkable stability across a range of NaCl concentrations from 0.01 to 60 mM, maintaining a consistent SPR peak at 530 nm, with negligible peak variation, as depicted in Figure S3A. In contrast, sodium citrate-reduced AuNPs (SC-AuNPs) showed the characteristic SPR peak only within a narrower NaCl concentration range (0.01 to 10 mM). At higher salinity levels, particularly at 60 mM, the characteristic SPR peak significantly diminished, as shown in Figure S3B. This comparative analysis underscores the superior stability of TA-AuNPs-3 over SC-AuNPs across various ionic strengths, advocating their applicability in diverse analytical settings. Moreover, both TA-AuNPs-3 and SC-AuNPs demonstrated comparable stability within the pH range of 5.0 to 9.0. Additionally, TA-AuNPs-3 exhibited sustained stability, maintaining their characteristic SPR peak at 530 nm from day 1 to day 20, underscoring their suitability and enduring efficacy for bioanalytical detection systems. Considering their proven long-term stability and reliability, TA-AuNPs-3 were chosen as the preferred probe for $H_2O_2$ detection in this study.

**3.2. Colorimetric Determination of $H_2O_2$.** Prior research has established that in the presence of $H_2O_2$, iodide ions ($I^-$) can effectively etch gold nanorods.[37,38] Specifically, this reaction process leads to the formation of $I_2$ molecules, which then interact with additional $I^-$ ions to create $I_3^-$ ions. These $I_3^-$ ions are instrumental in the etching and subsequent oxidation of gold nanorods. Leveraging insights from these studies, we propose a detection mechanism for $H_2O_2$ utilizing the TA-AuNPs-3/$I^-$ system, as delineated in Scheme 1.

To substantiate our hypothesis, we examined the UV−vis spectra of TA-AuNPs-3 under diverse conditions, as illustrated in Figure 2. Observations from Figure 2 reveal that the mere addition of TA-AuNPs-3 with $I^-$ (indicated by the red spectrum) or TA-AuNPs-3 with $H_2O_2$ (indicated by the blue spectrum) does not lead to the generation of a characteristic $I_3^-$ peak at 350 nm. In the case of $I^-$ addition, the UV−vis slight change is attributed to the change in the TA-AuNPs-3 dielectrics because of the displacement of the outer TA layer by $I^-$ ions. Conversely, the simultaneous addition of TA-AuNPs-3, $I^-$, and $H_2O_2$ results in a pronounced $I_3^-$ peak at 350 nm (indicated by the green spectrum), enabling the quantification of $H_2O_2$ based on this distinct peak.

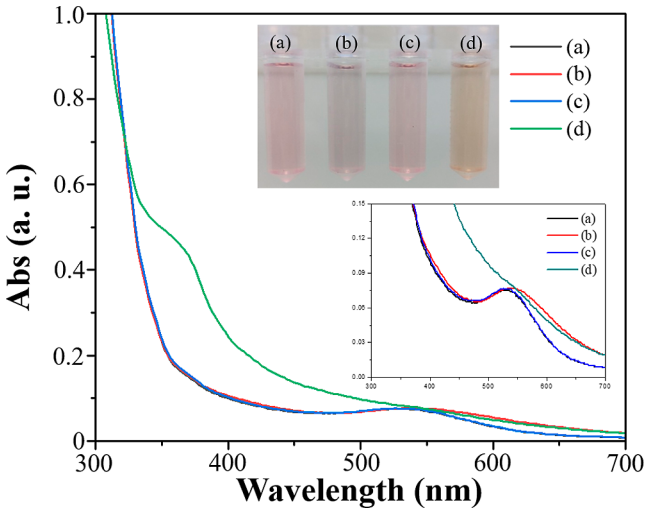


**Figure 2.** UV−vis spectral analysis of TA-AuNPs-3 in the (a) absence and (b−d) presence of various reactants: (b) 0.1875 M KI, (c) 0.2 mM $H_2O_2$, and (d) 0.1875 M KI and 0.2 mM $H_2O_2$ combined. Inset: visual comparison was made through photographic images of the respective AuNP solutions. Photograph courtesy of Chun-Hsiang Peng. Copyright 2024.

Further analysis presented in Figure S4A demonstrates that introducing KI to TA-AuNPs-3 causes the displacement of the outer TA layer by $I^-$ ions, resulting in the aggregation of TA-AuNPs-3/$I^-$, which signifies the existence of interaction. Conversely, as depicted in Figure S4B, introducing $H_2O_2$ to TA-AuNPs-3 neither modifies their size nor leads to aggregation. Nevertheless, the concurrent introduction of TA-AuNPs-3, KI, and $H_2O_2$ initiates the conversion of $I^-$ ions into $I_3^-$ ions, which subsequently oxidize the TA-AuNPs-3 to $AuI_2^-$ ions, rendering the nanoparticles undetectable in TEM imagery. This phenomenon is further supported by the findings in Figure S4C,D, where after adding $I^-$ ions and $H_2O_2$, both hydrodynamic diameter and zeta potential nearly reach zero, signifying the conversion of TA-AuNPs-3 into $AuI_2^-$ ions. Thus, the generation of $I_3^-$ is exclusive to the joint addition of TA-AuNPs-3, KI, and $H_2O_2$, affirming the validity of our proposed detection mechanism, as depicted in Scheme 1.

**3.3. Sensing Mechanism and Steady-State Kinetic Study.** Next, we employed theoretical simulations using VASP to examine the adsorption energies of $I^-$ and $H_2O_2$ on TA-AuNPs. These simulations aimed to elucidate the interaction dynamics of $I^-$ and $H_2O_2$ on the surface of TA-AuNPs, as depicted in Figure S5. The adsorption energy for $H_2O_2$ on the TA-AuNPs surface was determined by using the following formula

$$E_{\mathrm{Ads}(H_2O_2)} = E_{H_2O_2@Au} - (E_{Au(111)} + E_{H_2O_2}) \quad (2)$$

To calculate this energy, the individual values for $E_{H2O2@Au}$, $E_{Au(111)}$, and $E_{H2O2}$ were first computed and then inserted into the formula. The results show that $E_{Au(111)}$ is 466.498 eV and $E_{H2O2}$ is 18.139 eV, with further data in Table 2. For the adsorption energy of iodine, we used the formula

$$E_{\mathrm{Ads(I)}} = E_{I@Au} - \left(E_{Au(111)} + \frac{E_{I_2}}{2}\right) \quad (3)$$

Here, the energies for $E_{Au(111)}$, $E_{I@Au}$, and $E_{I2}$ were separately computed. In the VASP framework, direct calculation of a single iodine atom's energy may yield inaccuracies; thus, we derived it from the calculated energy of the $I_2$ molecule by dividing it by two. This approach yielded the adsorption energies. Subsequently, $E_{Au(111)}$ was maintained at 466.498 eV, and $E_{I2}$ was calculated to be 26.397 eV, with additional specifics outlined in Table 2. The comparative analysis reveals that the adsorption energy for $I^-$ is notably more significant than that for $H_2O_2$, with the latter's energies being below 0.1 eV, indicating a tendency toward physisorption. Conversely, the substantial adsorption energy associated with $I^-$ points to chemisorption. Notably, the adsorption site with a fcc structure shows the highest energy, suggesting that adsorption at this site is the most stable. Consequently, our computational findings demonstrate that $I^-$ ions exhibit higher adsorption energies on TA-AuNPs surfaces, inferring that the oxidation process is inclined toward the Eley−Rideal mechanism.



https://doi.org/10.1021/acsomega.4c05826
ACS Omega 2024, 9, 38217−38226

Table 2. Simulation Adsorption Energy for the TA-AuNPs/KI/$H_2O_2$ System

| site | top | bridge | fcc | hcp |
|---|---|---|---|---|
| $E_{H2O2@Au}$ | −484.687 | −484.67 | −484.699 | −484.686 |
| $E_{ads(H2O2)}$ | −0.05018 | −0.03360 | −0.06222 | −0.04933 |
| $E_{I@Au}$ | −468.478 | −468.801 | −468.930 | −468.842 |
| $E_{ads(I)}$ | −0.6599 | −0.9836 | −1.1125 | −1.025 |

The elemental composition of TA-AuNPs-3, without and with the $I^-$ and $H_2O_2$ systems, was examined via XPS. As illustrated in Figure S6A(a), the full scan spectrum of TA-AuNPs-3 distinctly unveils the $Au_{4f}$ peak, confirming the successful reduction of $Au^{3+}$ to TA-AuNPs-3 by TA, as evidenced by the high-resolution $Au_{4f}$ spectrum [Figure S6A(b)], which delineates peaks at 84.0 eV for $Au_{4f7/2}$ and 87.4 eV for $Au_{4f5/2}$. Figure S6B(a) demonstrates the full scan spectrum of TA-AuNPs-3/$I^-$, highlighting both $Au_{4f}$ and $I_{3d}$ peaks. Notably, the high-resolution spectra [Figure S6B(b,c)] reveal the presence of $I_{3d7/2}$ (618.6 eV) and $I_{3d5/2}$ (630.0 eV) peaks, alongside a reduction in $Au_{4f}$ peak intensity. For the full scan spectrum of TA-AuNPs-3/$I^-$/$H_2O_2$, as shown in Figure S6C(a), it predominantly displays $I_{3d}$ peaks, with subsequent high-resolution analysis [Figure S6C(b,c)] confirming the absence of $Au_{4f}$ peaks and increased intensity for $I_{3d7/2}$ and $I_{3d5/2}$ peaks, underscoring the dynamic surface chemistry involved. This observation suggests that Au was successfully oxidized to $Au^+$, and concurrently, $I^-$ was oxidized to $I_3^-$. The atomic percentages (%) of the elements for the TA-AuNPs under different conditions are summarized in Table 3.

Table 3. Atomic Percentage (%) of Au and I Elements for TA-AuNPs under Different Conditions

| conditions | Au (%) | I (%) |
|---|---|---|
| TA-AuNPs-3 | 4.4 | 0 |
| TA-AuNPs-3/$I^-$ | 1.4 | 1.9 |
| TA-AuNPs-3/$I^-$/$H_2O_2$ | <0.1 | 4.4 |

Drawing from the previously discussed findings, we can delineate the hypothesized sensing mechanism for $H_2O_2$ utilizing the TA-AuNPs-3/$I^-$ system as follows: As demonstrated in eq 4, the introduction of KI leads to displacement of the TA groups on the surface of TA-AuNPs-3 by $I^-$ ions. This process results in the adsorption of $I^-$ ions onto TA-AuNPs-3. Following this, introducing $H_2O_2$ initiates a reaction between the TA-AuNPs-3 surface-adsorbed $I^-$ and $H_2O_2$, generating $I_2$ that becomes affixed to TA-AuNPs-3, as shown in eq 5. This $I_2$ on the surface further interacts with $I^-$ ions from the solution, culminating in the formation of $I_3^-$ on TA-AuNPs-3, as shown in eq 6. The bound $I_3^-$ ions then react with more $I^-$ ions on the surface of TA-AuNP-3. According to the theory of iodine leaching of gold, $I_3^-$ reacts with TA-AuNP-3 to produce $AuI_2^-$, as shown in eq 7 and detailed in the subsequent equations.[39−41]

$$TA - AuNPs + I^- \rightarrow I^-\cdots\cdots AuNPs \quad (4)$$

$$2I^-\cdots\cdots AuNPs + H_2O_2 + 2H^+ \rightarrow I_2\cdots\cdots AuNPs + 2H_2O \quad (5)$$

$$I^- + I_2\cdots\cdots Au - AuNPs \rightarrow I_3^-\cdots\cdots AuNPs \quad (6)$$

$$I^-\cdots\cdots AuNPs + I_3^-\cdots\cdots Au \rightarrow 2AuI_2^- \quad (7)$$

Next to the steady-state kinetic study, at ambient temperature, TA-AuNPs-3 solutions were prepared to $1.1 \times 10^{-7}$ M. Into this mixture, 0.9 mL of deionized water, 0.5 mL of $H_2O_2$ (25 mM), and 0.5 mL of KI at various concentrations were added. The varying reaction times were monitored, and their absorption spectra were captured by using a UV−vis spectrophotometer, specifically noting the absorption peak at 350 nm. The initial formation rate of $I_3^-$ was determined based on this peak, creating a logarithmic plot correlating the rate with KI concentration. As illustrated in Figure S7A, the derived slope of this line stands at 0.61, representing the reaction order concerning KI.[25,26] In a parallel setup, TA-AuNPs-3 were prepared to $1.1 \times 10^{-7}$ M and combined with 0.9 mL deionized water, 0.5 mL of KI, and 0.5 mL of $H_2O_2$ at different concentrations, all within a 2.0 mL microcentrifuge tube. The absorption spectra from these mixtures were also recorded over various time intervals, centering once more on the peak at 350 nm for the initial $I_3^-$ rate calculation. This data facilitated the generation of another log−log plot, illustrating the rate against $H_2O_2$ concentration. As demonstrated in Figure S7B, the linear fit yielded a slope of 0.69, indicative of the reaction order for $H_2O_2$. As per the data fitting shown in Figure S8, the computed average rate constant ($k$) is 0.217 $M^{-1.3}/s$.[25,26]

### 3.4. Optimum Conditions and Sensing Performance.

At ambient temperature, TA-AuNPs-3 solutions (the concentration of the freshly prepared TA-AuNPs-3 (1×) was estimated to be $2.2 \times 10^{-6}$ M) were adjusted to concentrations ranging from 1/20× to 5/20× in 2 mL microcentrifuge tubes. Each sample received additions of 0.5 mL of KI (0.75 M) and 0.5 mL of $H_2O_2$ (25 mM), culminating in a total volume of 2 mL. After a reaction duration of 10 min, absorbance at the 350 nm wavelength was recorded and labeled as A. Concurrently, a control group lacking $H_2O_2$ was measured at the same wavelength to acquire absorbance $A_0$. Analysis revealed that a decrease in the TA-AuNP-3 concentration leads to an increase in the $(A - A_0)/A_0$ ratio (Figure 3A). With the highest signal boost observed at the 1/20× dilution level of TA-AuNPs-3, this concentration was chosen as the optimal for $H_2O_2$ detection, equivalent to a TA-AuNPs-3 concentration of $1.1 \times 10^{-7}$ M. Under similar conditions, the TA-AuNPs-3 were set to a concentration of $1.1 \times 10^{-7}$ M and combined with 0.5 mL of KI at various concentrations (5.0, 2.5, 1.0, 0.75, and 0.50 M) and 0.5 mL of 25 mM $H_2O_2$. Absorbance at 350 nm was measured, denoted as A, with a control set without $H_2O_2$ for absorbance $A_0$. The findings suggest that increasing KI concentrations shift the reaction toward $I_3^-$ formation, with the reaction optimization occurring at 0.75 M KI due to the superior interaction with TA-AuNPs-3, as indicated by enhanced absorbance values (Figure 3B). Regarding the reaction time, according to the data and as illustrated in Figure 3C, there is minimal change in signal enhancement after 30 min, and the smallest standard deviation occurs at this time point. Thus, for improved stability of the detection system, a duration of 30 min was established as the ideal reaction time for $H_2O_2$ assessment. Lastly, the experiments were performed


https://doi.org/10.1021/acsomega.4c05826
ACS Omega 2024, 9, 38217−38226

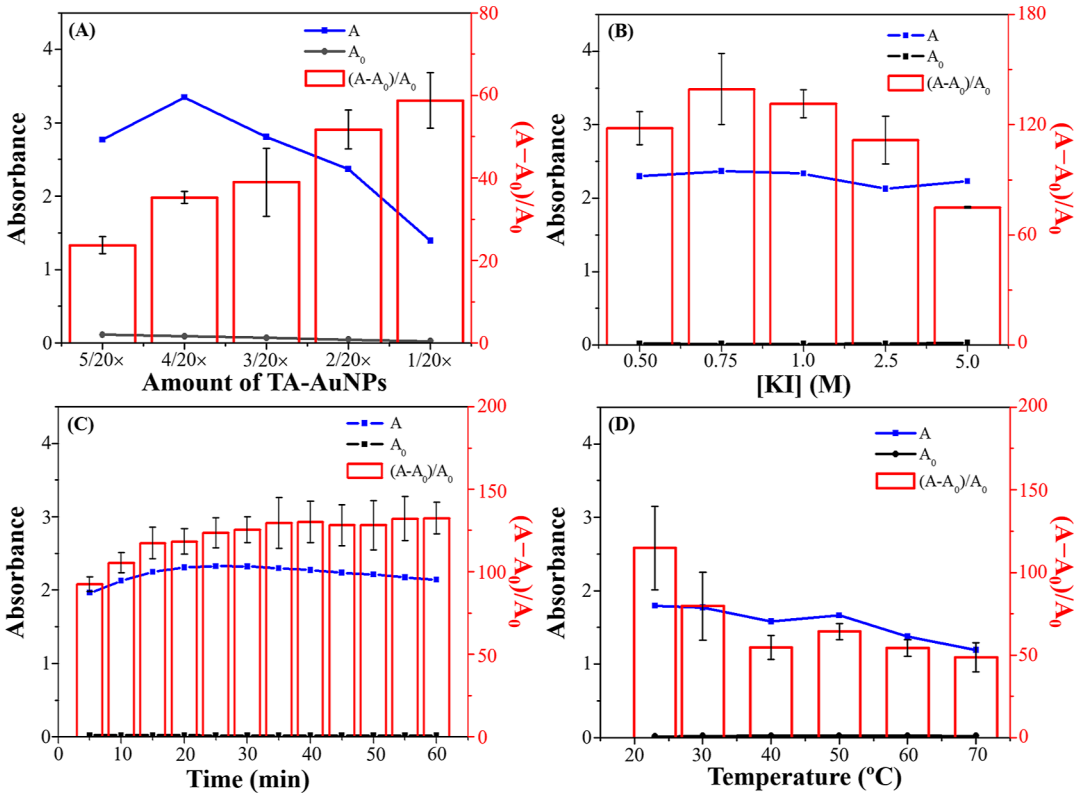


**Figure 3.** Determination of optimal conditions for $H_2O_2$ detection using the TA-AuNPs-3/$I^-$ system, analyzing variables: (A) TA-AuNPs-3 concentration, (B) KI concentration, (C) reaction time, and (D) assay temperature.

at various temperatures: 23, 30, 40, 50, 60, and 70 °C using TA-AuNPs-3 at $1.1 \times 10^{-7}$ M, mixed with 0.5 mL of 0.75 M KI and 0.5 mL of 25 mM $H_2O_2$. Absorbance was again logged at 350 nm, marked as A, alongside a control set for each temperature without $H_2O_2$ to obtain $A_0$. As demonstrated in Figure 3D, elevated temperatures lead to the decomposition of $H_2O_2$ into water and oxygen, diminishing the oxidative effect on $I^-$ and, therefore, not significantly altering its conversion to yellow $I_3^-$. Hence, 23 °C was selected as the optimum temperature for $H_2O_2$ detection.

Figure 4A demonstrates that the proposed TA-AuNPs-3/$I^-$ system exhibits high selectivity for $H_2O_2$ (200 $\mu$M) compared to other interferences, including $Na^+$, $K^+$, $Mg^{2+}$, $Ca^{2+}$, AA, UA, GLY, GSH, and BSA, each at a concentration of 500 $\mu$M. Under the optimal conditions, this analytical setup offers a detection spectrum between 150 and 275 $\mu$M, presents a limit of detection (LOD) of 7.33 $\mu$M at a S/N ratio of 3.0 ($\text{LOD} = \frac{3 \times \sigma_{\text{blank}}}{\text{slope}} = \frac{3 \times 0.0242}{0.0099} = 7.33\ \mu\text{M}$), and achieves a correlation coefficient ($R^2$) of 0.97, as elucidated in Figure 4B. In comparison to previous literature, while the detection linearity and sensitivity of the proposed system may be somewhat limited, its utility remains promising for glucose level assessment in human samples, a potential further validated in subsequent implementations.

**3.5. Application.** As illustrated in Scheme 1, integration of the TA-AuNPs-3/$I^-$ system with GOx facilitates glucose detection. This efficacy stems from glucose undergoing oxidation by GOx to yield gluconic acid and $H_2O_2$. The resultant $H_2O_2$ engages in the previously described reaction mechanism to make TA-AuNPs-3/$I^-$ form $I_3^-$, enabling the indirect quantification of glucose levels. Owing to the specific action of GOx on glucose to produce $H_2O_2$, the system demonstrates high specificity toward glucose, as evidenced in Figure 5A. In optimized conditions, this combined system with GOx exhibits a glucose detection range of 200 to 350 $\mu$M, with a $R^2$ of 0.96 and a LOD of 10.0 $\mu$M at a S/N ratio of 3.0 ($\text{LOD} = \frac{3 \times \sigma_{\text{blank}}}{\text{slope}} = \frac{3 \times 0.011}{0.0033} = 10.0\ \mu\text{M}$), as shown in Figure 5B. In contrast, SC-AuNPs show a linear detection range of 175−275 $\mu$M for $H_2O_2$ with a LOD of 58.8 $\mu$M and a linear detection range of 70−120 $\mu$M for glucose with a LOD of 12.9 $\mu$M, as shown in Figure S9. These results indicate that the TA-AuNP detection system offers a broader detection range and lower LODs for both $H_2O_2$ and glucose compared to those of the SC-AuNP system. Therefore, the TA-AuNP system exhibits higher sensitivity and broader applicability.

For practical applications, human urine was diluted and employed as a solvent for preparing glucose solutions of various concentrations. Under the optimized conditions, a quantitative calibration curve for glucose in human urine was generated. Experimental results, as shown in Table 4, indicate that the system is anticipated to deliver recoveries between 96.6 and 102.0%, with a relative standard deviation (RSD) from 3.00 to 8.34%, confirming the suitability of the proposed system for biochemical sample testing.

Table 5 compares the colorimetric analysis of glucose using nanomaterial-based sensors. Our TA-AuNPs-3/$I^-$ system exhibits several advantageous properties: (1) Enhanced stability and simplicity: the one-pot synthesis method using TA simplifies the production process, providing stable TA-AuNPs without the need for complex purification steps. This stability is crucial for reliable and reproducible bioanalytical applications. (2) Acceptable sensitivity: the TA-AuNPs-3/$I^-$ system demonstrates low LODs of 7.33 $\mu$M for $H_2O_2$ and 10.0 $\mu$M for glucose, which are competitive with or superior to


https://doi.org/10.1021/acsomega.4c05826
ACS Omega 2024, 9, 38217−38226

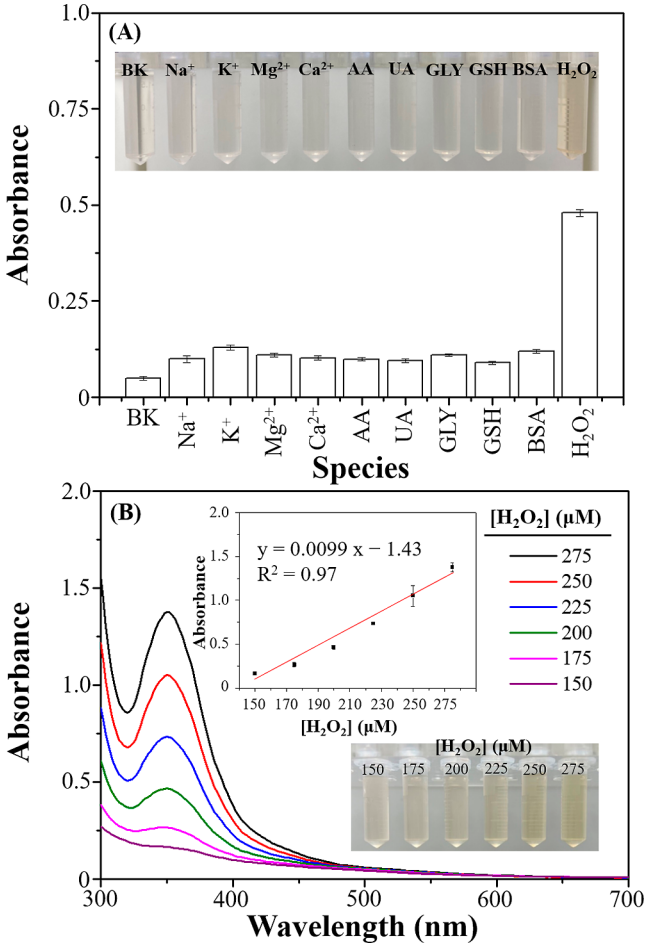


**Figure 4.** (A) Assessment of selectivity for $H_2O_2$ using the TA-AuNPs-3/$I^-$ system. Photographic images show the color changes in TA-AuNPs-3/$I^-$ solutions corresponding to different ions and molecules. Photograph courtesy of Chen-Yu Chueh. Copyright 2024. (B) UV−vis spectral response of the TA-AuNPs-3/$I^-$ system across different $H_2O_2$ concentrations (150−275 $\mu$M). Inset: correlation was observed between the absorbance at 350 nm and $H_2O_2$ concentrations. Accompanying images display color variations in TA-AuNPs-3/$I^-$ solutions corresponding to $H_2O_2$ levels. Photograph courtesy of Chun-Hsiang Peng. Copyright 2024.

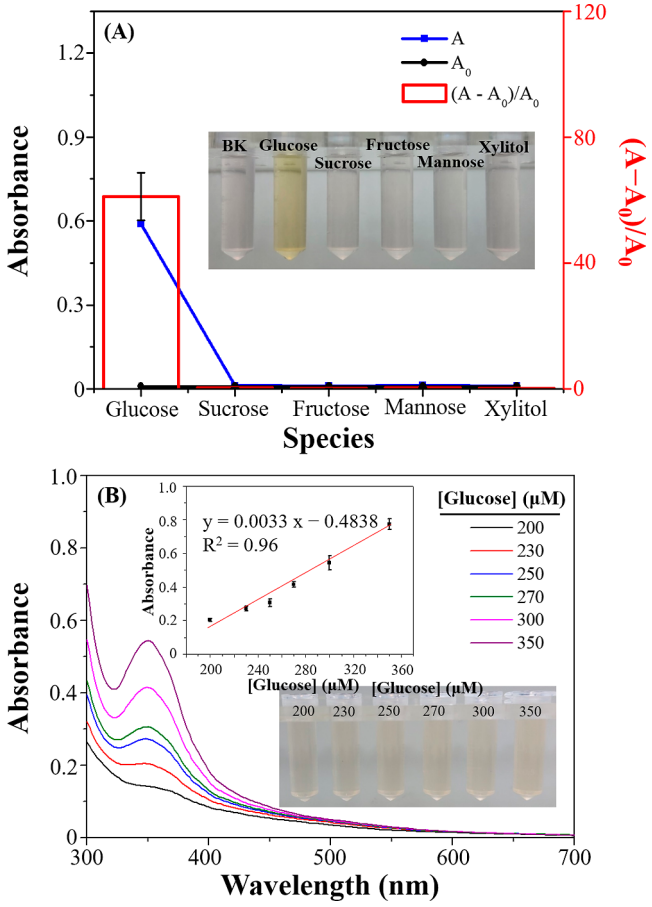


**Figure 5.** (A) Assessment of selectivity for glucose using the GOx/TA-AuNPs-3/$I^-$ system. Photographic images show the color changes in GOx/TA-AuNPs-3/$I^-$ solutions corresponding to different sugar molecules. Photograph courtesy of Tsung-Yuan Wang. Copyright 2024. (B) UV−vis spectra for the GOx/TA-AuNPs-3/$I^-$ system across varying glucose concentrations (200−350 $\mu$M). Inset: Linear relationship exists between absorbance at 350 nm and glucose concentrations. Photographic images showcase the color changes in GOx/TA-AuNPs-3/$I^-$ solutions corresponding to different glucose levels. Photograph courtesy of Tsung-Yuan Wang. Copyright 2024.

similar probes. (3) Versatile application: the utility of the system extends to detecting biomolecules such as glucose by integrating GOx. This dual functionality for $H_2O_2$ and glucose detection showcases the versatility of the probe, making it suitable for various bioanalytical and clinical settings. (4) Real-world applicability: the application of this method to actual urine samples yielded spiked recoveries ranging from 96.6 to 102.0% and RSDs between 3.00 and 8.34%, highlighting its practical efficacy and reliability in real-world bioanalytical challenges.

## 4. CONCLUSIONS

This study proposed a novel $H_2O_2$ detection method utilizing one-pot synthesized TA-AuNPs, simplifying preparation processes by eliminating the need for postsynthesis purification. The TA-AuNPs in this study demonstrate higher stability than those synthesized using sodium citrate, resulting in broader applicability. The synthesis method described here is simpler and does not require special purification steps, significantly reducing preparation costs and lowering the expertise needed for operation, thus enhancing its practical applicability. The method capitalizes on the distinctive

**Table 4. Glucose Spiked Recovery and RSD for the TA-AuNPs-3/KI System**

| sample | glucose ($\mu$M) | detected ($\mu$M) | recovery (%) | RSD (%) |
|---|---|---|---|---|
| **urine** | 200 | 204 | 101.9 | 3.00 |
| | 230 | 222 | 96.6 | 4.62 |
| | 250 | 247 | 98.8 | 5.55 |
| | 270 | 266 | 98.6 | 5.71 |
| | 300 | 306 | 102.0 | 8.34 |

**Table 5. Comparison of the Colorimetric Analysis of Glucose by Nanomaterial-Based Sensors**

| probe | linear range ($\mu$M) | LOD ($\mu$M) | real sample | ref |
|---|---|---|---|---|
| FPBA-AgNP | 100−2000 | 89 | serum | 42 |
| $MoS_2$ | 5−90 | 1.2 | serum | 43 |
| AuNPs | 13.8−110 | 9.8 | urine | 44 |
| $V_2O_5$ | 10−2000 | 10 | none | 45 |
| TA-AuNPs | 200−350 | 10 | urine | this work |


https://doi.org/10.1021/acsomega.4c05826
ACS Omega 2024, 9, 38217−38226

oxidative interaction between $I^-$ ions on the surface of TA-AuNPs and $H_2O_2$, leading to a visible color shift at 350 nm, indicative of $I_3^-$ formation. This approach enables precise quantification of $H_2O_2$ with a LOD of 7.33 $\mu$M, achieved under optimal conditions: $1.1 \times 10^{-7}$ M TA-AuNPs-3 and 0.75 M KI at 23 °C for 30 min. Furthermore, the versatility of the system is demonstrated through its application in glucose detection, reaching a LOD of 10.0 $\mu$M, thus showcasing its potential in biochemical assays. The effectiveness of this system is confirmed through its application to actual human urine samples for glucose analysis, yielding accurate and clinically relevant results with detection ranges from 250 to 300 $\mu$M, recovery rates from 96.6 to 102.0%, and minimal variability (RSD $\leq$ 8.34%). This integration of innovative detection and practical utility marks a significant advancement in bioanalytical techniques, offering an efficient, cost-effective, and versatile solution for concurrent monitoring of $H_2O_2$ and glucose with important implications for healthcare diagnostics and environmental monitoring. In addition, because the method is also dependent on the amount of $H_2O_2$, our approach might be applicable to the detection of various substrates or the activity of various enzymes when combined with enzymatic reactions.

## ■ ASSOCIATED CONTENT

### Supporting Information

The Supporting Information is available free of charge at https://pubs.acs.org/doi/10.1021/acsomega.4c05826.

Zeta potential of TA-AuNPs-3; characterization of TA-AuNPs-3; comparative UV−vis spectral analysis of TA-AuNPs-3 and SC-AuNPs assessing NaCl tolerance; TEM images of TA-AuNPs-3 at different conditions; computational simulation illustrating the interaction energy profiles; XPS analysis of the TA-AuNPs-3/$I^-$/$H_2O_2$ system; kinetic study of the TA-AuNPs-3/$I^-$/$H_2O_2$ system; steady-state kinetic fitting for the TA-AuNPs-3/$I^-$/$H_2O_2$ system; and detecting performances of $H_2O_2$ and glucose using SC-AuNPs (PDF)

## ■ AUTHOR INFORMATION


### Corresponding Author

**Yang-Wei Lin** − *Department of Chemistry, National Changhua University of Education, Changhua City 50007, Taiwan;* orcid.org/0000-0001-8667-0811; Phone: +886-4-7211190; Email: linywjerry@cc.ncue.edu.tw

### Authors

**Chun-Hsiang Peng** − *Department of Chemistry, National Changhua University of Education, Changhua City 50007, Taiwan*

**Tsung-Yuan Wang** − *Department of Chemistry, National Changhua University of Education, Changhua City 50007, Taiwan*

**Chen-Yu Chueh** − *Department of Chemistry, National Changhua University of Education, Changhua City 50007, Taiwan*

**Tsunghsueh Wu** − *Department of Chemistry, University of Wisconsin-Platteville, Platteville, Wisconsin 53818-3099, United States*

**Jyh-Pin Chou** − *Department of Physics, National Changhua University of Education, Changhua City 50007, Taiwan;* orcid.org/0000-0001-8336-6793

**Mei-Yao Wu** − *School of Post-baccalaureate Chinese Medicine, China Medical University, Taichung 40424, Taiwan*

Complete contact information is available at: https://pubs.acs.org/10.1021/acsomega.4c05826

### Author Contributions

⊥C.-H.P. and T.-Y.W. contributed equally to this work.


### Notes

The authors declare no competing financial interest.

## ■ ACKNOWLEDGMENTS

This study was supported by the National Science and Technology Council (NSTC) under contracts (112-2113-M-018-005), (113-2113-M-018-001), and (112-2813-C-018-050-M) and the Ministry of Education Teaching Practice Research Program under contract (PMS1120077).

## ■ REFERENCES


(1) Shen, M.-H.; Singh, R. K. Detoxification of aflatoxins in foods by ultraviolet irradiation, hydrogen peroxide, and their combination-a review. *LWT* **2021**, *142*, 110986.

(2) Silva, K. J. S.; Sabogal-Paz, L. P. A 10-year critical review on hydrogen peroxide as a disinfectant: could it be an alternative for household water treatment? *Water Supply* **2022**, *22* (12), 8527−8539.

(3) Xie, B.; Yang, X.; Zhang, R.; Guo, J.; Chen, Z.; He, Y. Hollow and porous $Fe_3C$-NC nanoballoons nanozymes for cancer cell $H_2O_2$ detection. *Sens. Actuators, B* **2021**, *347*, 130597.

(4) Cheng, D.; Li, P.; Zhu, X.; Liu, M.; Zhang, Y.; Liu, Y. Enzyme-free electrochemical detection of hydrogen peroxide based on the three-dimensional flower-like Cu-based metal organic frameworks and MXene nanosheets. *Chin. J. Chem.* **2021**, *39* (8), 2181−2187.

(5) Duanghathaipornsuk, S.; Farrell, E. J.; Alba-Rubio, A. C.; Zelenay, P.; Kim, D.-S. Detection technologies for reactive oxygen species: fluorescence and electrochemical methods and their applications. *Biosensors (Basel)* **2021**, *11* (2), 30.

(6) Ahmad, T.; Iqbal, A.; Halim, S. A.; Uddin, J.; Khan, A.; El Deeb, S.; Al-Harrasi, A. Recent advances in electrochemical sensing of hydrogen peroxide ($H_2O_2$) released from cancer cells. *Nanomaterials* **2022**, *12* (9), 1475.

(7) Ling, Z.; Yang, L.; Zhang, W.; Yao, T.; Xu, H. Detection of food contaminants: A review of established rapid analytical techniques and their applications and limitations. *Food Saf. Health* **2024**, *2* (1), 72−95.

(8) Wu, Q.; Chen, H.; Fang, A.; Wu, X.; Liu, M.; Li, H.; Zhang, Y.; Yao, S. Universal multifunctional nanoplatform based on target-induced in situ promoting Au seeds growth to quench fluorescence of upconversion nanoparticles. *ACS Sens.* **2017**, *2* (12), 1805−1813.

(9) Su, J.; Zhang, S.; Wang, C.; Li, M.; Wang, J.; Su, F.; Wang, Z. A fast and efficient method for detecting $H_2O_2$ by a dual-locked model chemosensor. *ACS Omega* **2021**, *6* (23), 14819−14823.

(10) Li, L.; Liu, X.; Zhu, R.; Wang, B.; Yang, J.; Xu, F.; Ramaswamy, S.; Zhang, X. $Fe^{3+}$-doped aminated lignin as peroxidase-mimicking nanozymes for rapid and durable colorimetric detection of $H_2O_2$. *ACS Sustainable Chem. Eng.* **2021**, *9* (38), 12833−12843.

(11) Zhou, Z.; Li, Y.; Su, W.; Gu, B.; Xu, H.; Wu, C.; Yin, P.; Li, H.; Zhang, Y. A dual-signal colorimetric and near-infrared fluorescence probe for the detection of exogenous and endogenous hydrogen peroxide in living cells. *Sens. Actuators, B* **2019**, *280*, 120−128.

(12) Govindaraj, M.; Srivastava, A.; Muthukumaran, M. K.; Tsai, P.-C.; Lin, Y.-C.; Raja, B. K.; Rajendran, J.; Ponnusamy, V. K.; Arockia Selvi, J. Current advancements and prospects of enzymatic and non-enzymatic electrochemical glucose sensors. *Int. J. Biol. Macromol.* **2023**, *253*, 126680.

(13) Thatikayala, D.; Ponnamma, D.; Sadasivuni, K. K.; Cabibihan, J.-J.; Al-Ali, A. K.; Malik, R. A.; Min, B. Progress of advanced nanomaterials in the non-enzymatic electrochemical sensing of glucose and $H_2O_2$. *Biosensors (Basel)* **2020**, *10* (11), 151.
(14) Hu, Y.; Hojamberdiev, M.; Geng, D. Recent advances in enzyme-free electrochemical hydrogen peroxide sensors based on carbon hybrid nanocomposites. *J. Mater. Chem. C* **2021**, *9* (22), 6970−6990.
(15) Sohrabi, H.; Maleki, F.; Khaaki, P.; Kadhom, M.; Kudaibergenov, N.; Khataee, A. Electrochemical-based sensing platforms for detection of glucose and $H_2O_2$ by porous metal-organic frameworks: A review of status and prospects. *Biosensors (Basel)* **2023**, *13* (3), 347.
(16) Sun, Y.; Li, P.; Zhu, Y.; Zhu, X.; Zhang, Y.; Liu, M.; Liu, Y. In situ growth of $TiO_2$ nanowires on $Ti_3C_2$ MXenes nanosheets as highly sensitive luminol electrochemiluminescent nanoplatform for glucose detection in fruits, sweat and serum samples. *Biosens. Bioelectron.* **2021**, *194*, 113600.
(17) Chen, Q.; Liu, M.; Zhao, J.; Peng, X.; Chen, X.; Mi, N.; Yin, B.; Li, H.; Zhang, Y.; Yao, S. Water-dispersible silicon dots as a peroxidase mimetic for the highly-sensitive colorimetric detection of glucose. *Chem. Commun.* **2014**, *50* (51), 6771−6774.
(18) Lin, Y.-W.; Huang, C.-C.; Chang, H.-T. Gold nanoparticle probes for the detection of mercury, lead and copper ions. *Analyst* **2011**, *136* (5), 863−871.
(19) Lin, Y.-W.; Liu, C.-W.; Chang, H.-T. DNA functionalized gold nanoparticles for bioanalysis. *Anal. Methods* **2009**, *1* (1), 14−24.
(20) Liu, D.-M.; Dong, C. Gold nanoparticles as colorimetric probes in food analysis: Progress and challenges. *Food Chem.* **2023**, *429*, 136887.
(21) Lu, M.; Su, L.; Luo, Y.; Ma, X.; Duan, Z.; Zhu, D.; Xiong, Y. Gold nanoparticle etching induced by an enzymatic-like reaction for the colorimetric detection of hydrogen peroxide and glucose. *Anal. Methods* **2019**, *11* (37), 4829−4834.
(22) Khan, M. M.; Cho, M. H. Positively charged gold nanoparticles for hydrogen peroxide detection. *BioNanoScience* **2018**, *8*, 537−543.
(23) Li, X.; Lv, J.; Zhao, J.; Ling, G.; Zhang, P. Swellable colorimetric microneedles for glucose detection based on glucose oxidase-like gold nanoparticles. *Anal. Chim. Acta* **2024**, *1288*, 342152.
(24) Ji, X.; Li, Q.; Su, R.; Wang, Y.; Qi, W. Peroxidase-mimicking hierarchically organized gold particles for glucose detection. *Langmuir* **2023**, *39* (9), 3216−3224.
(25) Barrera, L. A.; Escobosa, A. C.; Alsaihati, L. S.; Noveron, J. C. Conducting a low-waste iodine clock experiment on filter paper to discern the rate law. *J. Chem. Educ.* **2019**, *96* (1), 165−168.
(26) Limpanuparb, T.; Ruchawapol, C.; Sathainthammanee, D. Clock reaction revisited: catalyzed redox substrate-depletive reactions. *J. Chem. Educ.* **2019**, *96* (4), 812−818.
(27) Kresse, G.; Furthmüller, J. Efficient iterative schemes for *ab* initio total-energy calculations using a plane-wave basis set. *Phys. Rev. B* **1996**, *54* (16), 11169−11186.
(28) Kresse, G.; Furthmüller, J. Efficiency of *ab*-initio total energy calculations for metals and semiconductors using a plane-wave basis set. *Comput. Mater. Sci.* **1996**, *6* (1), 15−50.
(29) Perdew, J. P.; Burke, K.; Wang, Y. Generalized gradient approximation for the exchange-correlation hole of a many-electron system. *Phys. Rev. B* **1996**, *54* (23), 16533−16539.
(30) Blöchl, P. E. Projector augmented-wave method. *Phys. Rev. B* **1994**, *50* (24), 17953−17979.
(31) Kresse, G.; Joubert, D. From ultrasoft pseudopotentials to the projector augmented-wave method. *Phys. Rev. B* **1999**, *59* (3), 1758−1775.
(32) Grimme, S. Density functional theory with London dispersion corrections. *Wiley Interdiscip. Rev.: Comput. Mol. Sci.* **2011**, *1* (2), 211−228.
(33) Choudhary, K.; Tavazza, F. Convergence and machine learning predictions of Monkhorst-Pack *k*-points and plane-wave cut-off in high-throughput DFT calculations. *Comput. Mater. Sci.* **2019**, *161*, 300−308.
(34) Aromal, S. A.; Philip, D. Facile one-pot synthesis of gold nanoparticles using tannic acid and its application in catalysis. *Phys. E* **2012**, *44* (7−8), 1692−1696.
(35) Miola, M.; Multari, C.; Kostevšek, N.; Gerbaldo, R.; Laviano, F.; Verné, E. Tannic-acid-mediated synthesis and characterization of magnetite-gold nanoplatforms for photothermal therapy. *Nanomedicine* **2023**, *18* (20), 1331−1342.
(36) Luo, Y.; Barwa, T. N.; Dempsey, E.; Karthik, R.; Shim, J.; Sukanya, R.; Breslin, C. B. Electrochemical detection of sulfanilamide using tannic acid exfoliated $MoS_2$ nanosheets combined with reduced graphene oxide/graphite. *Environ. Res.* **2024**, *248*, 118391.
(37) Weng, G.; Dong, X.; Li, J.; Zhao, J. Halide ions can trigger the oxidative etching of gold nanorods with the iodide ions being the most efficient. *J. Mater. Sci.* **2016**, *51*, 7678−7690.
(38) Weng, G.; Dong, X.; Zhao, J.; Li, J.; Zhu, J.; Zhao, J. Selective oxidative etching of CTAC-stabilized multi-branched gold nanoparticles: application in spectral sensing of iodide ions. *J. Nanopart. Res.* **2018**, *20*, 256.
(39) Tang, N.; Shan, Y.; Zhang, R.; Meng, X. Sensitive and simple detection of trace hydrogen peroxide based on a resonance light scattering assay. *Anal. Methods* **2015**, *7* (20), 8750−8756.
(40) Zhang, Z.; Li, H.; Zhang, F.; Wu, Y.; Guo, Z.; Zhou, L.; Li, J. Investigation of halide-induced aggregation of Au nanoparticles into spongelike gold. *Langmuir* **2014**, *30* (10), 2648−2659.
(41) Davis, A.; Tran, T. Gold dissolution in iodide electrolytes. *Hydrometallurgy* **1991**, *26* (2), 163−177.
(42) Cao, K.; Jiang, X.; Yan, S.; Zhang, L.; Wu, W. Phenylboronic acid modified silver nanoparticles for colorimetric dynamic analysis of glucose. *Biosens. Bioelectron.* **2014**, *52*, 188−195.
(43) Lin, T.; Zhong, L.; Guo, L.; Fu, F.; Chen, G. Seeing diabetes: Visual detection of glucose based on the intrinsic peroxidase-like activity of $MoS_2$ nanosheets. *Nanoscale* **2014**, *6* (20), 11856−11862.
(44) Chaudhary, A.; Gupta, A.; Nandi, C. K. Anisotropic gold nanoparticles for the highly sensitive colorimetric detection of glucose in human urine. *RSC Adv.* **2015**, *5* (51), 40849−40855.
(45) Sun, J.; Li, C.; Qi, Y.; Guo, S.; Liang, X. Optimizing colorimetric assay based on $V_2O_5$ nanozymes for sensitive detection of $H_2O_2$ and glucose. *Sensors* **2016**, *16* (4), 584.


https://doi.org/10.1021/acsomega.4c05826
*ACS Omega* 2024, 9, 38217−38226